

Table-top interferometry on extreme time and wavelength scales

S. Skruszewicz¹, A. Przystawik¹, D. Schwickert¹, M. Sumfleth¹, M. Namboodiri¹, V. Hilbert², R. Klas^{2,3}, P. Gierschke⁴, V. Schuster², A. Vorobiov⁵, C. Haunhorst⁵, D. Kip⁵, J. Limpert^{2,3,4}, J. Rothhardt^{2,3,4}, and T. Laarmann^{1,6,*}

¹Deutsches Elektronen-Synchrotron DESY, Notkestraße 85, Hamburg, 22607, Germany

²Institute of Applied Physics, Friedrich-Schiller-University Jena, Albert-Einstein-Straße 15, 07745 Jena, Germany

³Helmholtz Institute Jena, Fröbelstieg 3, 07743 Jena, Germany

⁴Fraunhofer Institute for Applied Optics and Precision Engineering, Albert-Einstein-Straße 7, 07745 Jena, Germany

⁵Faculty of Electrical Engineering, Helmut Schmidt University, Holstenhofweg 85, Hamburg 22043, Germany.

⁶The Hamburg Centre for Ultrafast Imaging CUI, Luruper Chaussee 149, Hamburg 22761, Germany.

*tim.laarmann@desy.de

ABSTRACT

Short-pulse metrology and dynamic studies in the extreme ultraviolet (XUV) spectral range greatly benefit from interferometric measurements. In this contribution a Michelson-type all-reflective split-and-delay autocorrelator operating in a quasi amplitude splitting mode is presented. The autocorrelator works under a grazing incidence angle in a broad spectral range (10 nm – 1 μ m) providing collinear propagation of both pulse replicas and thus a constant phase difference across the beam profile. The compact instrument allows for XUV pulse autocorrelation measurements in the time domain with a single-digit attosecond precision and a useful scan length of about 1 ps enabling a decent resolution of $E/\Delta E = 2000$. Its performance for selected spectroscopic applications requiring moderate resolution at short wavelengths is demonstrated by characterizing a sharp electronic transition at 26.6 eV in Ar gas. The absorption of the 11th harmonic of a frequency-doubled Yb-fiber laser leads to the well-known $3s3p^64p^1P^1$ Fano resonance of Ar atoms. We benchmark our time-domain interferometry results with a high-resolution XUV grating spectrometer and find an excellent agreement. The common-path interferometer opens up new opportunities for short-wavelength femtosecond and attosecond pulse metrology and dynamic studies on extreme time scales in various research fields.

1 Introduction

Interferometry in the extreme ultraviolet spectral range (XUV) plays a key role in attosecond pulse metrology for more than 20 years¹. It has led to a wide range of applications ranging from attosecond spectroscopy² to coherent diffractive imaging on the nanoscale using table-top sources^{3,4}. It is the capability of interferometric methods to access the relative phases and amplitudes of interfering waves known from optics that is used to track propagating quantum objects, such as charge or spin waves in matter on extremely short distances and corresponding ultrafast time scales⁵. Along these lines, phase-sensitive light wave metrology in time and frequency domain goes hand-in-hand with advanced coherent spectroscopy and imaging applications using electrons, ions or photons as observable. Experimental breakthroughs, such as watching real-time electronic wave packet dynamics in atoms⁶, orbital tomography in molecules⁷ and optical coherence tomography of solids⁸, rely on controlling or detecting the phase of an electromagnetic wave with high precision^{9,10}.

In typical spectroscopic studies, the signal intensity is recorded, while the phase information is lost. High-resolution XUV spectrometers provide a resolution ($E/\Delta E$), which depends on the diffraction grating period, i. e. the number of illuminated grooves and on the wavelength of the light. Typically, it is on the order of $E/\Delta E = 10^3$ ¹¹, while special custom-made gratings can reach a resolution of up to a few times 10^4 . Although these optical elements are not off-the-shelf and very expensive, they are now utilized in large scale soft x-ray synchrotron beamlines especially for spectroscopic techniques demanding high resolution, such as resonant inelastic x-ray scattering (RIXS) (see for instance¹²). An alternative approach is Fourier-transform (FT) spectroscopy. By its nature, it enables characterization of radiation in both time and frequency domain using a single instrument. The spectral resolution of such a system depends on the maximum optical-path difference between replicas of the beam propagating in both interferometer arms¹³. Thus, it can exceed the spectral resolution of the grating-based analyzers by orders of magnitude, if very large delays can be used¹⁴. Moreover, the resolution is uniform across the entire photon energy range, which usually is not the case for grating-based spectrometers.

The standard geometry of FT spectrometers employs the typical Michelson-interferometer beam path. Its essential component is a beam splitter, which permits for splitting the field amplitude of the incoming laser pulse in two identical parts propagating along two perpendicular interferometer arms. Combining the two replicas with parallel wavefronts on the detector maximizes the interference contrast. The transfer of the two-arm concept into the short-wavelength range has been demonstrated for specific wavelengths based on multi-layer optics^{15,16}. The main challenge for performing FT spectroscopy in the XUV and beyond is, however, the design of a beam splitter covering a broad spectral range, reaching high transmission and maintaining a plane wavefront. To meet these challenges, alternative schemes have been developed in recent years based on either engineering two source points in close proximity with variable pulse delay or special split-and-delay units, applied to a single radiation source. In the former scheme, two mutually coherent XUV pulses separated in space and time can be generated by harmonic generation from two laser pulses focused into a gas jet with the same separation¹⁷⁻¹⁹. The latter concept is based on a conventional half-mirror split-and-delay unit^{20,21}. Both approaches have already been employed to characterize attosecond pulse trains in time and frequency domain^{19,22} and for spectroscopy at synchrotron radiation facilities¹⁴. The major drawback of these concepts is that the two XUV pulses do not propagate collinearly. Due to the partial overlap in the far field, only a small fraction of the lateral beam profile can be used to evaluate the interference signal. Because the pulses interfere at small skew angles, the phase between beams changes continuously along the intersection path in the focal volume. Consequently, the interference contrast in these non-collinear geometries is typically much weaker than in Michelson-type interferometers.

In this contribution we demonstrate FT spectroscopy in the XUV spectral range by employing a recently developed Michelson-type all-reflective split-and-delay autocorrelator design²³. The instrument is based on two interleaved lamellar mirrors, which generate two replicas of XUV pulses propagating collinearly. It enables quasi amplitude division, resolves interferometric autocorrelation signals and can be applied in modern Ramsey-like experimental schemes²⁴. It implies that the device can be used to acquire phase information in some cases, for instance, if implemented in nonlinear detection schemes that go beyond measuring field-autocorrelation traces in spectroscopic applications. Of course, the latter are better off at continuous or pseudo-continuous sources like synchrotrons¹⁴. The common-path laser interferometer allows for tight focusing of phase-coherent pulse replicas while keeping the fringe contrast at maximum in the focal volume. This unique capability is essential for nonlinear coherent spectroscopic applications and ultrashort pulse metrology.

2 Experimental Setup

The experiment utilizes a table-top high-harmonic source driven by Yb-fiber-laser technology and delivering short pulses with high photon flux in the XUV. Such sources can provide significantly higher repetition rates than the currently operating free-electron lasers based on superconducting linear accelerators²⁵ and offer very high temporal resolution due to the intrinsically small timing jitter²⁶. Here we use a high harmonic source, which is conceptually similar to the one presented in²⁷, but operating at a reduced repetition rate of 100kHz. A 20 W average power Yb-fiber laser providing 250 fs pulses at 1030 nm is frequency doubled in a 1 mm thick BBO crystal. The resulting 200 fs, 515 nm pulses at 10 W average power are post compressed to sub-20 fs using a nonlinear hollow-core fiber with a subsequent chirped-mirror compressor. High-harmonic generation (HHG) is driven by focusing these pulses to a spot size of 90 μm into an Ar gas jet resulting in a generated photon flux of $\approx 2 \cdot 10^{15}$ photons/s in the 11th harmonic (H11) at 26.5 eV photon energy. Subsequently, separation of the driving laser and the generated XUV radiation is achieved using two grazing-incidence plates²⁸, with an XUV reflectivity of 55% each, and additional 200 nm thick aluminum filters with a measured XUV transmission of 20%²⁹. Spatial and spectral characterization of the generated XUV radiation is performed by using the 90°-reflection of a removable 1 μm aluminum foil by means of a flat-field grating spectrometer equipped with a CCD camera.

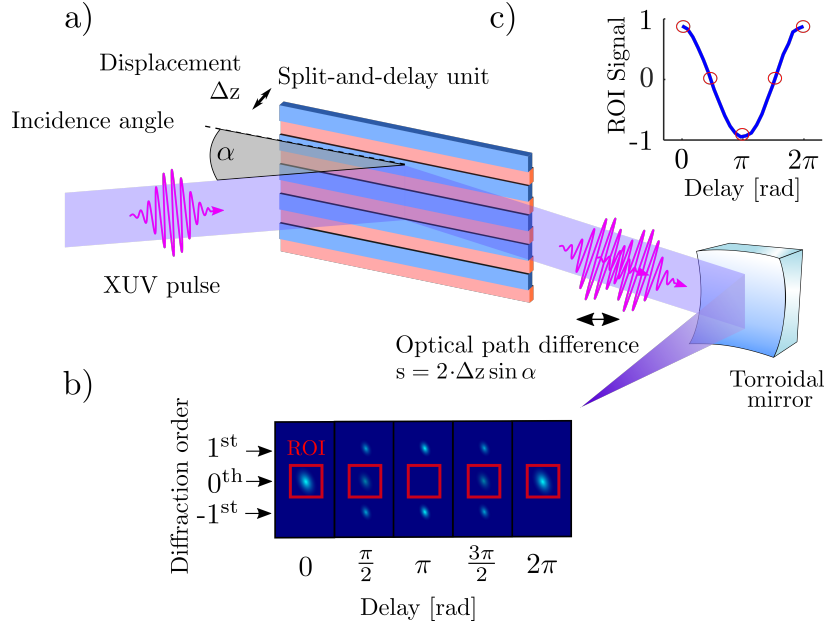


Figure 1. Illustration of the experimental realization for XUV Fourier-transform spectroscopy. (a) An XUV pulse is reflected at $\alpha = 8^\circ$ incidence angle from a Michelson-type split-and-delay unit. The two coherent copies propagating collinearly are focused by a toroidal mirror onto a Ce:YAG scintillator. (b) In the focal plane at the Ce:YAG scintillator the diffraction orders of the lamellae can be resolved. Integrating the signal from the region-of-interest (red box, ROI) encompassing the 0th diffraction order as a function of relative phase delay yields the field-autocorrelation trace of the light source. (c) The Fourier transform of the sketched interferogram provides the spectrum of the XUV source.

Fig. 1 shows a schematic overview of the optical beam passing the FT instrument. The key element is the split-and-delay unit (SDU). It consists of two interleaved lamellar mirrors splitting the wavefront of the incoming XUV pulse uniformly across the beam profile. The design was suggested by Strong and Vanasse in the late 50's to overcome the absence of beam splitters in the far-infrared spectral range³⁰. In the 90's Möller proposed to extend the principle of lamellar mirrors to the high energy range³¹. The special mirror assembly in the present realization is cut from a silicon wafer and is coated with a 30nm thick nickel layer. Its period is $d = 250\mu\text{m}$. The mechanical stability of the SDU is essential for interferometry at short wavelengths. In order to measure a high-quality interferogram of H11 at $\lambda = 46.8\text{nm}$ the relative position of the reflective elements should be known to a precision better than $\approx 10\text{nm}$, i.e. $\approx \lambda/4$. This is on the order of the background vibration in the laboratory, which is typically monitored during the measurements. The position of the reflective lamellar surface in the movable interferometer arm is controlled by 3-axes piezo-driven motors with nanometer precision. Building on previous demonstrations^{32,33}, the setup is advanced by integrating three commercial laser interferometers (SmarAct) enabling position measurement of the lamellar optics at repetition rates up to 40kHz for online feedback control and offline FT data tagging. These refinements improve the precision of the relative lamellar-mirror displacement by 1-2 orders of magnitude, thereby improving the contrast in the recorded interferograms. This precision and stability is crucial for FT spectroscopy in the XUV spectral range. The XUV light is reflected from the autocorrelator mirrors at the grazing-incidence angle of $\alpha = 8^\circ$. The SDU provides collinear propagation of the two coherent pulse replicas with variable delay controlled by translating the movable lamellar mirror with nanometer and attosecond precision, respectively. Note that the optical path difference (OPD) is given by

$$s = 2 \cdot \Delta z \cdot \sin \alpha, \quad (1)$$

with Δz being the mirror displacement. For instance, a displacement of $\Delta z = 1\text{nm}$ corresponds to about $s = 280\text{pm}$, which results in a time delay between the copies of XUV pulses of only $\Delta t = 0.93\text{as}$.

Upon reflection from the lamellar-mirror assembly, the XUV beam is focused onto a Ce:YAG scintillator by a toroidal mirror with a focal length of $f = 5.3\text{m}$. The wavefronts of each partial beam are parallel in each diffraction order. Thus, the temporal interference generated in the far-field depends only on the longitudinal displacement of the lamellar mirrors. The diffraction maxima are separated by $\Delta r = \lambda f/d$, where λ is the central wavelength, d is the lamellar period and f is the focal length³². The maximum intensity continuously slips between even and odd diffraction orders as we scan the relative phase (time) delay

between the two beams. At delay $\tau = 0$ the maximum intensity is reached in 0th order, whereas for $\tau = \pi$ the odd diffraction orders are enhanced with maximum contrast due to the collinear beam propagation in the common-path interferometer³³. It allows for tight focusing of phase-coherent pulse replicas, while keeping the fringe contrast at maximum in the focal point. This unique capability is essential for nonlinear coherent spectroscopic applications striving to unravel ultrafast quantum phenomena in matter by detecting electrons and ions generated in the focal volume. For cameras and similar detectors this is not strictly true however, since it is in principle possible to select a small partial fraction of the fringe system. In the present experiment, the fluorescence signal from the scintillator is recorded by a CMOS camera. In order to obtain the field-autocorrelation (AC) trace of the light source, we integrate the signal intensity in the region-of-interest (ROI) encompassing the 0th-order diffraction maximum. Note that the 0th-order maximum consist of all frequencies selected by a plane multi-layer mirror, which was designed for a photon energy of 26.6 eV and installed behind the lamellar-mirror assembly in front of the vacuum chamber hosting the detectors. In data processing, we account for laser intensity fluctuations by normalizing the AC signal to the overall signal intensity recorded by the CMOS detector. Additionally, we apply a centroiding algorithm correcting the position of the image center in the far-field. This allows for correction of small beam-pointing fluctuations remaining from the beam-stabilization system of the optical driving laser. The statistical analysis of the recorded scintillator images gives a spatial jitter in the XUV focal plane of $\Delta x = 15 \mu\text{m}$ horizontally and $\Delta y = 60 \mu\text{m}$ (FWHM) vertically, i.e. in dispersion direction (see the inset in Fig. 2). This is approximately a factor of 3 smaller than the beam waist at focus assuming diffraction-limited optics and Gaussian XUV beams. Beam-pointing instabilities on this order of magnitude are usually insignificant for applications using electron and ion spectrometers. The field autocorrelation $A_F(\tau)$ is defined by

$$\begin{aligned} A_F(\tau) &= \int_{-\infty}^{+\infty} |E_{XUV}(t) + E_{XUV}(t - \tau)|^2 dt \\ &= 2 \cdot \int_{-\infty}^{+\infty} |E_{XUV}(t)|^2 dt + 2 \cdot \text{Re} \int_{-\infty}^{+\infty} E_{XUV}^*(t) E_{XUV}(t - \tau) dt, \end{aligned} \quad (2)$$

where $E_{XUV}(t)$ represents the complex electric field of the XUV pulse and τ is the delay between two laser pulses. Note that the first term refers to the pulse energy and the second is the field AC. Thus, Eq.(2) is the foundation of Fourier-transform spectroscopy. Measuring the interferogram $A_F(\tau)$ is equivalent to measuring the filtered spectrum of the harmonic source. The recorded signal is periodically modulated as a function of time delays and its Fourier transform yields the spectrum. We emphasize that the temporal profile (chirp) of the XUV pulse cannot be determined from $A_F(\tau)$. However, the spectral bandwidth provides the transform-limited pulse duration and vice versa. For a drive pulse with a sufficiently small chirp, the interferogram can visualize the number of attosecond bursts in one attosecond pulse train emitted during the HHG process as described in²².

The sampling energy width of the Fourier-transform spectrometer depends solely on the OPD between the two XUV pulse replicas

$$\Delta E \propto 1/L, \quad (3)$$

where L is the maximum optical path difference that can be set in the autocorrelator. In our instrument the corresponding maximum useful mirror displacement of $\Delta z = 1 \text{ mm}$ at a grazing-incidence angle of $\alpha = 8^\circ$ results in $L = 278 \mu\text{m}$, which gives a maximum sampling energy width of $\Delta E = 4.5 \text{ meV}$. We note that for the device depicted in Fig. 1 the given resolution is limited intrinsically by the transient loss of the transverse overlap between the two beams reflected from the lamellar-mirror assembly for larger delays, i.e. the increasing mirror displacement resulting in parallel beam separation.

Due to the linearity of the Fourier transformation, the absolute calibration of the instrument requires only one reference spectral line. However, if this anchor point is not available, precise calibration of the delay time axis, i.e. the optical path difference in both interferometer arms, is still possible. It mainly requires exact knowledge of the grazing-incidence angle of the photon beam impinging on the lamellar-mirror assembly. Under these experimental conditions, an error of $\Delta\alpha = 0.1^\circ$ would result in a relative energy mismatch of about 1.2%, which is on the order of 300 meV for 26 eV photon energy. Note that this relative error is uniform and constant overall photon energies. In contrast, grating spectrometers separate wavelengths according to their characteristic diffraction angles. Thus, its absolute calibration requires series of well-known emission lines distributed over a broad spectral range e.g. equally spaced harmonics from an HHG process. Although the calibration of FT seems to be straightforward, we note in passing that it requires a well-collimated beam to start with. In our experiment we use a single toroidal mirror as a collimator. It is known that a toroid produces coma aberration, which we resolve in the

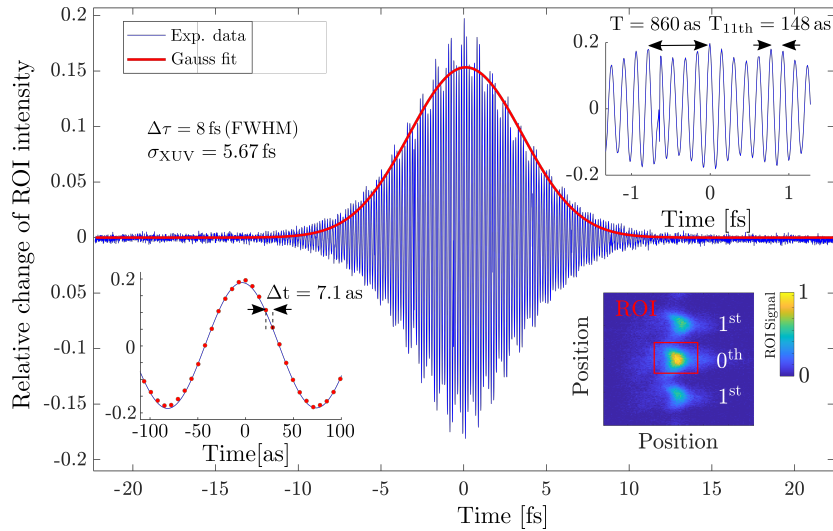


Figure 2. Linear auto-correlation trace of the HHG source (blue line) measured with the Ce:YAG scintillator accumulating 50 ms (5000 laser shots) per time step. A typical scintillator camera image of the diffraction orders is shown in the bottom right. The interferogram is derived by integrating the ROI (red square) and normalizing it to the intensity recorded by the entire CMOS detector. For sake of clarity we plot the difference between this signal and the average over the full delay scan. The Gaussian envelope fitted to the data gives a width $\Delta\tau = 8$ fs (FWHM) corresponding to a transform-limited pulse length of $\sigma_{\text{XUV}} = 5.7$ fs. The magnifications show the field oscillations of the dominant 11th harmonic with a time period of $T_{11\text{th}} = 148$ as recorded with a sampling step size of $\Delta t = 7.1$ as. In addition a slower beating pattern with a period of $T = 860$ as can be resolved.

far-field image of the focal spot (Fig. 2). Obviously, any kind of aberration in the far-field reduces the interference contrast in the measurement and a complex optical system for its compensation could be applied. For instance, studies using three toroidal mirrors controlled by a genetic algorithm achieved coma-free micrometer-size focal spots³⁴. However, it is the strength of the current common-path interferometer that these aberrations do not play a role here. As we will see in the following, as long as individual diffraction orders can be resolved in the far-field image the quality of the interferograms is extremely good.

3 Results

The field AC trace of the HHG source is shown in Fig. 2. It reveals periodic, sine-like modulations multiplied with a Gaussian envelope. The interferogram is obtained by integrating the intensity of the 0th-order interference maximum and plotting the corresponding signal as a function of time delay between the two XUV pulses. A typical image recorded by the camera shows the 0th and 1st diffraction orders as displayed in the inset (on the bottom right). We fit a Gaussian envelope to the AC signal and obtain the autocorrelation width of $\Delta\tau = 8$ fs (FWHM). Thus, the transform-limited XUV pulse length derived from the measurement is $\sigma_{\text{XUV}} = \Delta\tau/\sqrt{2} = 5.67$ fs. Note that this is in excellent agreement with simulations of the HHG phase matching window³⁵ and the single-atom response³⁶, resulting in an XUV pulse duration of < 6 fs²⁷.

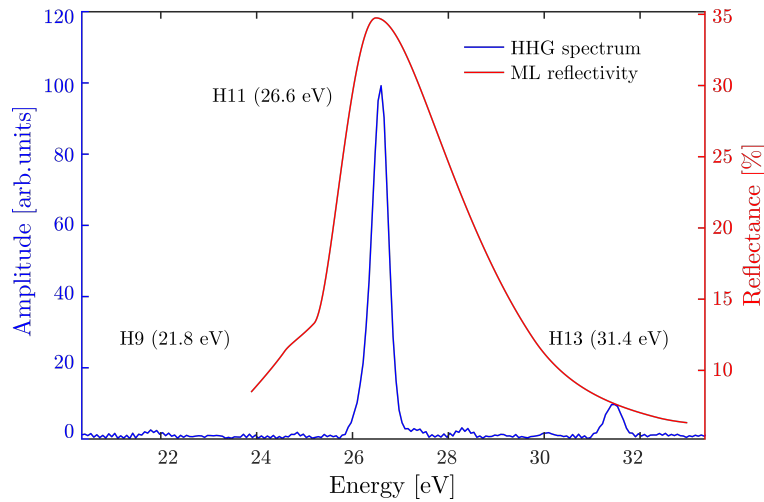


Figure 3. The XUV spectrum of the HHG source obtained by the Fourier transform of the AC signal (blue). The spectrum reveals a dominant contribution from H11 at 26.6 eV and two satellite peaks from H9 (21.8 eV) and H13 (31.4 eV). The amplitude of satellites is strongly suppressed by the reflectance of the multi-layer mirror (red), which is designed for H11.

In order to demonstrate the stability of the experimental setup we recorded interferograms with a sampling step size of $\Delta t = 7.1$ as. The clear oscillation shown in the zoom on the top right and bottom left in the Fig. 2 demonstrate the precise control of the relative phase of the harmonic pulses on the single-digit attosecond time scale. The field oscillation has a period $T_{11\text{th}} = 148$ as. In addition, a superimposed beating pattern is visible in the interferogram with a longer period of $T = 860$ as. It results from the neighboring harmonic orders H9 and H13, which pass the multi-layer mirror (ML) to some extent. It is worthwhile to note that this period matches the temporal separation of the individual bursts of attosecond laser pulses emitted at each optical half cycle of the driving laser pulse, whose visibility is suppressed due to the spectral filtering caused by the ML. At 515 nm drive wavelength, this corresponds to the observed time period of 860 as.

The Fourier transform of the recorded interferogram is displayed in Fig. 3. As expected, the spectrum shows a dominant peak at 26.6 eV (H11) with adjacent two weak satellite peaks at 21.8 eV (H9) and 31.4 eV (H13), respectively. This is in good agreement with the reflectivity curve of the multi-layer mirror, which was optimized for a photon energy of 26.6 eV selecting H11 and strongly suppressing the other frequencies from the harmonic comb.

To exploit the capacity of the FT instrument we spectrally narrow the 11th harmonic by filling an approximately 1 m long part of the vacuum chamber with Ar to increase its partial pressure, i.e. atom density. The presence of the Fano resonance in the photoabsorption continuum of Ar around 26.6 eV modifies the transmitted spectrum due to the spectrally narrow decrease of the absorption cross-section³⁷. We have selected this transition for our benchmark experiment, because the underlying spectral tailoring has been carefully analyzed previously by means of high-resolution grating-based spectroscopy³⁸. In Fig. 4 the results obtained from the FT measurements are compared with the spectrum recorded with the grating-based XUV spectrometer at two different conditions. The total absorption cross-section of Ar is plotted as a gray-dashed line. At a base pressure of (a) $p = 1 \cdot 10^{-5}$ mbar, i.e. negligible absorption due to the residual gas, the H11 energy bandwidth is $\Delta E = 430$ meV (FWHM). Its width is due to the short pulse duration (broad spectrum) of the 515 nm driving laser. Subsequently, we tailor the H11 transmission through the setup by utilizing the window-like Fano resonance. Therefore, we increase the Ar gas flow up to a backing pressure of (b) $p_{\text{Ar}} = 8 \cdot 10^{-2}$ mbar. Under this condition both spectrometer types resolve the asymmetric Fano profile with $\Delta E = 50$ meV (FWHM). The results are in very good agreement with the reported line width of $\Gamma = 76$ meV for the $3s3p^64p^1P^1$ Fano resonance measured at a synchrotron³⁹. Notably, the FT energy resolution is solely limited by the accessible delay range generated by the SDU as defined in Eq.(3). As described in section 2, the specifications of the FT instrument give an energy sampling width of $\Delta E = 4.5$ meV. This allows to achieve a resolution of about $\Delta E \approx 13$ meV with three sampling points per spectral line at 26.6 eV, which corresponds to $E/\Delta E = 2000$. Thus, the FT instrument offers comparable resolution as state-of-the-art high-resolution grating-based XUV spectrometers. The latter used in our experiment provides $\Delta E = 20$ meV²⁹ and its performance is in addition limited by the slit size, which compromises the signal strength on the detector.

An important parameter in Fourier-transform spectroscopy is the signal-to-noise ratio in the measured AC signal. To

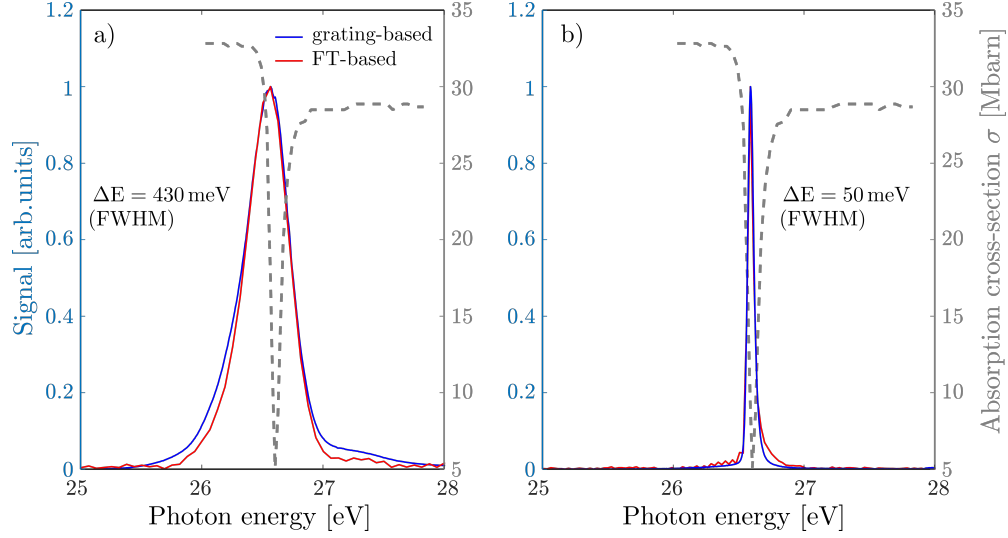


Figure 4. Spectra of the H11 emission resolved with a high-resolution XUV spectrometer (blue) and retrieved from FT measurement (red), respectively. (a) Spectra measured at the base pressure $p = 1 \cdot 10^{-5}$ mbar. (b) Spectra measured at the Ar backing pressure of $p_{\text{Ar}} = 8 \cdot 10^{-2}$ mbar. The total absorption cross-section of Ar is plotted as a gray dashed line³⁷. The sharp minimum in the absorption is due to the $3s3p^64p^1P^1$ Fano resonance, which locally modifies the total cross-section³⁹.

estimate the uncertainty limit for the position of spectral features we use the following empirical relation to estimate the line precision

$$\Delta\sigma [\text{eV}] = \frac{k}{\sqrt{N_W}} \frac{W}{S/N} \cdot \frac{1}{8065 \text{ cm}^{-1}}, \quad (4)$$

where k is a constant of the order of unity, which depends on the line shape. The value of N_W gives the number of statistically independent points in a fitted line width W (FWHM) and S/N is the signal-to-noise ratio⁴⁰. For the unperturbed H11 emission with $S/N = 40$, $N_W = 7$ and $W = 430 \text{ meV}$ the accuracy is about 4 meV . For the sharp Fano resonance the accuracy is about 0.7 meV . Obviously, this effect is significantly smaller than the current resolution limit set by the maximum beam path difference of one interferometer arm with respect to the other.

4 Summary

In this contribution we present benchmark experiments applying a compact common-path interferometer for Fourier-transform spectroscopy in the extreme ultraviolet spectral range. The key component of the device is a broad-bandwidth Michelson-type all-reflective split-and-delay unit. It allows to record field-autocorrelation traces at XUV wavelengths as a function of time delay between two coherent pulse replicas with single-digit attosecond resolution, while scanning delays up to 1 ps. The capacity of the technique is demonstrated by characterizing the 11th harmonic emission line of an ultrafast 515 nm driving laser. As we tailor the unperturbed 430 meV wide spectrum at 26.6 eV by the window-like $3s3p^64p^1P^1$ Fano resonance in Ar atoms we can clearly resolve the asymmetric lineshape with a natural width of $\Delta E = 50 \text{ meV}$ (FWHM) by sampling the data with an energy sampling width of 4.5 meV. We benchmark the results by comparing the data with experiments using a state-of-the-art grating-based high-resolution XUV spectrometer with a resolution of 20 meV and reach very good agreement. The power of interferometry for attosecond science becomes obvious when looking at the high-harmonic generation process in time domain. The recorded field-autocorrelation trace of the XUV light wave oscillation with a dominant time period of 148 as shows fingerprints of attosecond bursts emitted every half cycle of the optical drive pulse, i.e. every 860 as.

5 Outlook

A future challenge for applications requiring simultaneously high laser power density at focus position and a spectral resolution exceeding a few times 10^3 is to increase the effective surface of the lamellar-mirror assembly. This would support expanding the beam profile (larger numerical aperture) reflected from its surface and increasing the OPD without losing the spatial overlap and interference contrast, respectively. It calls for advanced engineering and materials design, because manufacturing

lamellar mirrors with larger area without distortion of the substrate on a level of 10 nm or less is demanding. Spatial distortions introduce phase errors in the reflected wavefronts, which reduce the interference contrast. Obviously, this is of great relevance for applications in the soft X-ray spectral range where the limits are truly on the single-digit nm scale. Therefore, we have started to develop special manufacturing protocols and nickel-coating procedures of the micro-machined silicon substrates for producing the next generation of lamellar-mirror assemblies for broadband soft x-ray applications. Recently, we have performed pioneering soft x-ray autocorrelation experiments, where we managed to control the relative phase of pulse replicas at 4.5 nm central wavelength on the corresponding few-attosecond timescale⁴¹. We could show that soft x-ray interferometry is a powerful tool to probe ultrafast correlated quantum phenomena, such as the excitation of Auger shake-up states with sub-cycle precision. Even without recording a complete autocorrelation trace and just measuring a few optical cycles we discovered that specific non-radiative Auger-decay channels show a relative time (phase) delay of only 3 as with respect to the driving light wave oscillation. This is among the fastest electronic processes ever measured demonstrating the power of phase-sensitive detection of interaction products using coherent soft x-ray pulse pairs.

Thus we can conclude that the performance of our interferometric autocorrelator at the heart of the FT spectrometer opens up a new window of opportunities for soft X-ray pulse metrology, dynamic studies and nonlinear coherent spectroscopy in matter, materials and in the life sciences. The development of table-top setups based on coherent femtosecond and attosecond sources is fundamental in this challenging field, as the access to free-electron lasers or other large-scale facilities is limited for obvious reasons. This is especially true considering the recent progress offered by high-harmonic generation sources pushing spectroscopic studies in time and frequency domain to the ultimate limit given by the uncertainty principle connecting temporal and energy resolution. Of particular interest is the so-called water window, which refers to the spectral range between the K-absorption edge of oxygen at a wavelength of 2.34 nm and the K-absorption edge of carbon at 4.4 nm corresponding to photon energies of 530 and 280 eV, respectively. Water is transparent to these soft x-rays, while carbon, nitrogen and other elements found in biomolecules are absorbing, which may allow to unravel biological functions with element-specificity in natural environment.

Funding.

This work was supported by the Fraunhofer Cluster of Excellence Advanced Photon Sources (CAPS), by the Innovation Pool of the Research Field Matter of the Helmholtz Association of German Research Centers in project (ECRAPS), by the Deutsche Forschungsgemeinschaft (DFG, German Research Foundation) through the Cluster of Excellence ‘Advanced Imaging of Matter’ (EXC 2056 - project ID 390715994), the collaborative research center ‘Light-induced Dynamics and Control of Correlated Quantum Systems’ (SFB-925 – project 170620586), the projects KI 482/20-1 and LA 1431/5-1 and by the Federal Ministry of Education and Research (BMBF) in project APPA R&D: Licht-Materie Wechselwirkung mit hochgeladenen Ionen (13N12082).

Disclosures.

The authors declare no conflicts of interest.

Data Availability.

The authors declare that the main data supporting the findings of this study are available within the article. Extra data are available from the corresponding author upon reasonable request.

References

1. Bellini, M. *et al.* Temporal coherence of ultrashort high-order harmonic pulses. *Phys. Rev. Lett.* **81**, 297–300, DOI: [10.1103/PhysRevLett.81.297](https://doi.org/10.1103/PhysRevLett.81.297) (1998).
2. Smirnova, O. *et al.* High harmonic interferometry of multi-electron dynamics in molecules. *Nature* **460**, 972–977, DOI: [10.1038/nature08253](https://doi.org/10.1038/nature08253) (2009).
3. Meng, Y. *et al.* Octave-spanning hyperspectral coherent diffractive imaging in the extreme ultraviolet range. *Opt. Express* **23**, 28960–28969, DOI: [10.1364/OE.23.028960](https://doi.org/10.1364/OE.23.028960) (2015).

4. Rothhardt, J., Tadesse, G. K., Eschen, W. & Limpert, J. Table-top nanoscale coherent imaging with XUV light. *J. Opt.* **20**, 113001, DOI: [10.1088/2040-8986/aae2d8](https://doi.org/10.1088/2040-8986/aae2d8) (2018).
5. González-Castrillo, A., Martín, F. & Palacios, A. Quantum state holography to reconstruct the molecular wave packet using an attosecond XUV–XUV pump-probe technique. *Sci. Rep.* **10**, 1–12, DOI: [10.1038/s41598-020-69733-1](https://doi.org/10.1038/s41598-020-69733-1) (2020).
6. Wituschek, A. *et al.* Tracking attosecond electronic coherences using phase-manipulated extreme ultraviolet pulses. *Nat. Commun.* **11**, 1–7, DOI: [10.1038/s41467-020-14721-2](https://doi.org/10.1038/s41467-020-14721-2) (2020).
7. Bertrand, J. B., Wörner, H. J., Salières, P., Villeneuve, D. M. & Corkum, P. B. Linked attosecond phase interferometry for molecular frame measurements. *Nat. Phys.* **9**, 174–178, DOI: [10.1038/nphys2540](https://doi.org/10.1038/nphys2540) (2013).
8. Fuchs, S. *et al.* Optical coherence tomography with nanoscale axial resolution using a laser-driven high-harmonic source. *Optica* **4**, 903–906, DOI: [10.1364/OPTICA.4.000903](https://doi.org/10.1364/OPTICA.4.000903) (2017).
9. Azoury, D., Krüger, M., Bruner, B. D., Smirnova, O. & Dudovich, N. Direct measurement of Coulomb-laser coupling. *Sci. Rep.* **11**, 1–9, DOI: [10.1038/s41598-020-79805-x](https://doi.org/10.1038/s41598-020-79805-x) (2021).
10. Uzan, A. J. *et al.* Spatial molecular interferometry via multidimensional high-harmonic spectroscopy. *Nat. Photonics* **14**, 188–194, DOI: [10.1038/s41566-019-0584-2](https://doi.org/10.1038/s41566-019-0584-2) (2020).
11. Wünsche, M. *et al.* A high resolution extreme ultraviolet spectrometer system optimized for harmonic spectroscopy and XUV beam analysis. *Rev. Sci. Instrum.* **90**, 023108, DOI: [10.1063/1.5054116](https://doi.org/10.1063/1.5054116) (2019).
12. Singh, A. *et al.* Development of the soft x-ray AGM–AGS RIXS beamline at the Taiwan photon source. *J. Synchrotron Radiat.* **28**, 977–986, DOI: [10.1107/S1600577521002897](https://doi.org/10.1107/S1600577521002897) (2021).
13. Bates, J. Fourier transform infrared spectroscopy. *Science* **191**, 31–37, DOI: [10.1126/science.1246596](https://doi.org/10.1126/science.1246596) (1976).
14. de Oliveira, N. *et al.* High-resolution broad-bandwidth Fourier-transform absorption spectroscopy in the VUV range down to 40 nm. *Nat. Photonics* **5**, 149–153, DOI: <https://doi.org/10.1038/nphoton.2010.314> (2011).
15. Hilbert, V. *et al.* An extreme ultraviolet Michelson interferometer for experiments at free-electron lasers. *Rev. Sci. Instrum.* **84**, 095111, DOI: [10.1063/1.4821146](https://doi.org/10.1063/1.4821146) (2013).
16. Hilbert, V. *et al.* Spatio-temporal coherence of free-electron laser radiation in the extreme ultraviolet determined by a Michelson interferometer. *Appl. Phys. Lett.* **105**, 101102, DOI: [10.1063/1.4895455](https://doi.org/10.1063/1.4895455) (2014).
17. Kovačev, M. *et al.* Extreme ultraviolet Fourier-transform spectroscopy with high order harmonics. *Phys. Rev. Lett.* **95**, 223903, DOI: [10.1103/PhysRevLett.95.223903](https://doi.org/10.1103/PhysRevLett.95.223903) (2005).
18. Tzallas, P., Charalambidis, D., Papadogiannis, N., Witte, K. & Tsakiris, G. D. Direct observation of attosecond light bunching. *Nature* **426**, 267–271, DOI: [10.1038/nature02091](https://doi.org/10.1038/nature02091) (2003).
19. Jansen, G. S. M., Rudolf, D., Freisem, L., Eikema, K. S. E. & Witte, S. Spatially resolved Fourier transform spectroscopy in the extreme ultraviolet. *Optica* **3**, 1122–1125, DOI: [10.1364/OPTICA.3.001122](https://doi.org/10.1364/OPTICA.3.001122) (2016).
20. Mashiko, H., Suda, A. & Midorikawa, K. All-reflective interferometric autocorrelator for the measurement of ultra-short optical pulses. *Appl. Phys. B* **76**, 525–530, DOI: [10.1007/s00340-003-1148-0](https://doi.org/10.1007/s00340-003-1148-0) (2003).
21. Mashiko, H. *et al.* Spatially resolved spectral phase interferometry with an isolated attosecond pulse. *Opt. Express* **28**, 21025–21034, DOI: [10.1364/OE.393922](https://doi.org/10.1364/OE.393922) (2020).
22. Chen, M.-C. *et al.* Generation of bright isolated attosecond soft x-ray pulses driven by multicycle midinfrared lasers. *Proc. Natl. Acad. Sci.* **111**, E2361–E2367, DOI: [10.1073/pnas.1407421111](https://doi.org/10.1073/pnas.1407421111) (2014). <https://www.pnas.org/content/111/23/E2361.full.pdf>.
23. Gebert, T. *et al.* Michelson-type all-reflective interferometric autocorrelation in the VUV regime. *New J. Phys.* **16**, 073047, DOI: [10.1088/1367-2630/16/7/073047](https://doi.org/10.1088/1367-2630/16/7/073047) (2014).
24. Eramo, R., Cavalieri, S., Corsi, C., Liontos, I. & Bellini, M. Method for high-resolution frequency measurements in the extreme ultraviolet regime: Random-sampling Ramsey spectroscopy. *Phys. Rev. Lett.* **106**, 213003, DOI: [10.1103/PhysRevLett.106.213003](https://doi.org/10.1103/PhysRevLett.106.213003) (2011).
25. Faatz, B. *et al.* Simultaneous operation of two soft x-ray free-electron lasers driven by one linear accelerator. *New J. Phys.* **18**, 062002, DOI: [10.1088/1367-2630/18/6/062002](https://doi.org/10.1088/1367-2630/18/6/062002) (2016).
26. Rothhardt, J. *et al.* High-repetition-rate and high-photon-flux 70 eV high-harmonic source for coincidence ion imaging of gas-phase molecules. *Opt. Express* **24**, 18133–18147, DOI: [10.1364/OE.24.018133](https://doi.org/10.1364/OE.24.018133) (2016).

27. Klas, R. *et al.* Ultra-short-pulse high-average-power Megahertz-repetition-rate coherent extreme-ultraviolet light source. *Photonix* **2**, 1–8, DOI: [10.1186/s43074-021-00028-y](https://doi.org/10.1186/s43074-021-00028-y) (2021).
28. Pronin, O. *et al.* Ultrabroadband efficient intracavity XUV output coupler. *Opt. Express* **19**, 10232–10240, DOI: [10.1364/OE.19.010232](https://doi.org/10.1364/OE.19.010232) (2011).
29. Hilbert, V., Tschernajew, M., Klas, R., Limpert, J. & Rothhardt, J. A compact, turnkey, narrow-bandwidth, tunable, and high-photon-flux extreme ultraviolet source. *AIP Adv.* **10**, 045227, DOI: [10.1063/1.5133154](https://doi.org/10.1063/1.5133154) (2020).
30. Strong, J. & Vanasse, G. A. Lamellar-grating far-infrared interferometer. *J. Opt. Soc. Am.* **50**, 113–118, DOI: [10.1364/JOSA.50.000113](https://doi.org/10.1364/JOSA.50.000113) (1960).
31. Möller, K. D. Wave-front-dividing array interferometers without moving parts for real-time spectroscopy from the IR to the UV. *Appl. Opt.* **34**, 1493–1501, DOI: [10.1364/AO.34.001493](https://doi.org/10.1364/AO.34.001493) (1995).
32. Usenko, S. *et al.* Split-and-delay unit for FEL interferometry in the XUV spectral range. *Appl. Sci.* **7**, 544, DOI: [10.3390/app7060544](https://doi.org/10.3390/app7060544) (2017).
33. Usenko, S. *et al.* Attosecond interferometry with self-amplified spontaneous emission of a free-electron laser. *Nat. Commun.* **8**, 15626, DOI: [10.1038/ncomms15626](https://doi.org/10.1038/ncomms15626) (2017).
34. Frassetto, F. *et al.* High-throughput beamline for attosecond pulses based on toroidal mirrors with microfocusing capabilities. *Rev. Sci. Instrum.* **85**, 103115, DOI: [10.1063/1.4898671](https://doi.org/10.1063/1.4898671) (2014).
35. Constant, E. *et al.* Optimizing high harmonic generation in absorbing gases: model and experiment. *Phys. Rev. Lett.* **82**, 1668–1671, DOI: [10.1103/PhysRevLett.82.1668](https://doi.org/10.1103/PhysRevLett.82.1668) (1999).
36. Lewenstein, M., Balcou, P., Ivanov, M. Y., L’huillier, A. & Corkum, P. B. Theory of high-harmonic generation by low-frequency laser fields. *Phys. Rev. A* **49**, 2117, DOI: [10.1103/PhysRevA.49.2117](https://doi.org/10.1103/PhysRevA.49.2117) (1994).
37. Madden, R. P., Ederer, D. L. & Codling, K. Resonances in the photo-ionization continuum of Ar I (20–150 eV). *Phys. Rev.* **177**, 136–151, DOI: [10.1103/PhysRev.177.136](https://doi.org/10.1103/PhysRev.177.136) (1969).
38. Rothhardt, J. *et al.* Enhancing the macroscopic yield of narrow-band high-order harmonic generation by Fano resonances. *Phys. Rev. Lett.* **112**, 233002, DOI: [10.1103/PhysRevLett.112.233002](https://doi.org/10.1103/PhysRevLett.112.233002) (2014).
39. Sorensen, S. L. *et al.* Argon 3s autoionization resonances. *Phys. Rev. A* **50**, 1218–1230, DOI: [10.1103/PhysRevA.50.1218](https://doi.org/10.1103/PhysRevA.50.1218) (1994).
40. Brault, J. High precision fourier transform spectrometry - the critical role of phase corrections. *Mikrochim Acta* **3**, 215–227, DOI: [10.1007/BF01201691](https://doi.org/10.1007/BF01201691) (1987).
41. Usenko, S. *et al.* Auger electron wave packet interferometry on extreme timescales with coherent soft x-rays. *J. Phys. B* **53**, 244008, DOI: [10.1088/1361-6455/abc661](https://doi.org/10.1088/1361-6455/abc661) (2020).